Evaluation of residual stress relaxation and its effect on fatigue strength of AISI 316L stainless steel ground surfaces: Experimental and numerical approaches

Adnen Laamouri [a,*], Habib Sidhom [b], Chedly Braham [c]

[a] Laboratoire de Mécanique, Matériaux et Procédés (LR99ES05), Institut Supérieur des Sciences Appliquées et de Technologie de Sousse, Université de Sousse, Cité Taffala, Avenue Ibn Khaldoun, 4003 Sousse, Tunisia
[b] Laboratoire de Mécanique, Matériaux et Procédés (LR99ES05), ESSTT, Université de Tunis, 5, Avenue Taha Husseïn, Montfleury, 1008 Tunis, Tunisia
[c] Laboratoire de Procédés et Ingénierie en Mécanique et Matériaux (PIMM, UMR CNRS 8006), ENSAM, 151, Boulevard de l'Hôpital Cedex 75013, Paris, France

Keywords:
Grinding
Fatigue
Residual stress relaxation
FE analyses
Cyclic hardening

A B S T R A C T

This paper is aimed at evaluating the residual stress relaxation and its effect on the fatigue strength of AISI 316L steel ground surfaces in comparison to electro-polished surfaces. An experimental evaluation was performed using 3-point and 4-point bending fatigue tests at $R_\sigma = 0.1$ on two sets of notched specimens finished by electro-polishing and grinding. The residual stress fields were measured at the notch root of specimens, before and after fatigue tests, by means of the X-ray diffraction technique. It was found a degradation of about −35% for the 4-point bending fatigue limit at 2×10^6 cycles of the ground specimens in comparison to the electro-polished ones. This degradation is associated with a slight relaxation of the grinding residual stresses which remain significant tensile stresses at the stabilized state. While under the 3-point bending test, these residual stresses relax completely and provoke a noticeable increase of the fatigue limit estimated at about 50% in comparison to the 4-point bending fatigue test. The numerical evaluation of residual stress relaxation was carried out by FE analyses of the cyclic hardening behaviour of the ground layer. The isotropic and nonlinear kinematic model proposed by Chaboche was used and calibrated for the base material and the ground layer. The results show that residual stresses relax to a stabilized state characterized by elastic-shakedown response. This stabilization is occurred after the first cycle of the 4-point bending test corresponding to the higher stress concentration ($K_{t\text{-}4p} = 1.66$), while it requires many cycles under the 3-point bending test corresponding to the lower stress concentration ($K_{t\text{-}3p} = 1.54$). The incorporation of stabilized residual stress values into the Dang Van's criterion has permitted to predict with an acceptable accuracy the fatigue limits under both bending modes.

1. Introduction

Generally, the various manufacturing processes such as machining, welding and all surface treatments induce residual stress gradients on the surface of metallic parts and structures [1,2]. It is well established that these stresses play an important role in service behaviour, particularly, in presence of cyclic loadings [3–6]. Indeed, the compressive stresses improve the fatigue strength, while tensile stresses are generally negative provided that they are stable.

However, residual stresses may partially or completely get relaxed during fatigue life [7–16]. In general, they reach a stabilized state when the cyclic loading is near fatigue limit. Therefore, the fatigue strength is widely related to the stabilized residual stresses acting in the most critical zone. It's well known that the residual stress relaxation is a complex phenomenon which may depend on interaction of several factors such as the amplitude of the applied cyclic stress, the loading mode, the number of cycles, the characteristics of the material, and the surface finishing process. Since the relaxation is associated with dislocation movement, it is therefore correlated to the plastic strain accumulation with the number of cycles. The main residual stress relaxation normally takes place in the first cycles, followed by further gradual relaxation during the life time [17]. The relaxation during the first cycle (quasi static loading) occurs when the superposition of the applied and residual stresses exceeds the monotonic yield strength of the material in tension and compression, while relaxation during successive cycles is related to the cyclic yield strength [13]. The latter is the most difficult and has attracted the attention of several researchers by using experimental and numerical approaches.

Therefore, the integration of residual stresses in fatigue strength predictive calculation, without considering their relaxation during operation, leads to inaccurate mathematical models for the reliability of the components and structures. The influence of residual

* Corresponding author. Tel.: +216 97219568; fax: +216 73332658.
E-mail address: adnen_laamouri@yahoo.fr (A. Laamouri).

Nomenclature

C, γ	material constants of the nonlinear kinematic hardening law
b, Q	material constants of the isotropic hardening law
dp	increment of the equivalent plastic strain
E	elastic modulus
f	yield surface defined by the Von Mises criterion
$I_{3p}(0)$, $I_{4p}(0)$	surface fatigue strength indicators corresponding to 3-point and 4-point bending tests, respectively
J_2	second invariant of the stress deviator tensor
k	initial yield stress in tension
K_f	fatigue stress concentration factor
K_t	stress concentration factor
$K_{t\text{-}3p}$, $K_{t\text{-}4p}$	stress concentration factors corresponding to 3-point and 4-point bending tests, respectively
P_{max}	maximum hydrostatic pressure
R	variable of the isotropic law
R_a	arithmetical mean roughness
R_t	maximum height of the roughness profile
R_σ, R_ε	loading ratios for stress-controlled and strain-controlled tests, respectively
s	standard deviation of the fatigue limit
$T.E.$	total elongation
$\underline{\underline{X}}$	variable of the nonlinear kinematic hardening law
z	coordinate of the depth in the notch root of fatigue specimens
α_0, β_0	material constants of the Dang Van's criterion
$\Delta\sigma_D$	fatigue limit at 2×10^6 cycles, expressed in terms of nominal stress range
$\Delta\varepsilon_t$	total strain range (i.e. elasto-plastic strain)
$\underline{\underline{\varepsilon}}^p$	plastic strain tensor
ν	Poisson's coefficient
σ_{UTS}	ultimate tensile strength
$\sigma_{Y0.2}$	0.2% yield strength
σ_F	fracture stress
$\underline{\underline{\sigma}}$	stress tensor
σ_{eq}	equivalent stress according to the Dang Van's criterion
$\sigma_R^{VM}(0)$	Von Mises equivalent stress corresponding to the surface residual stress state
$\underline{\underline{\sigma}}_R^*(z)$	Stabilized residual stress tensor for a z-depth
$\underline{\underline{\sigma}}_{app}(z,t)$	cyclic stress tensor due to an external applied loading at an instant t and for a z-depth
$\underline{\underline{\sigma}}_t(z,t)$	total stress tensor at an instant t and for a z-depth
$\sigma_{Rxx}(z)$, $\sigma_{Ryy}(z)$	in-depth profiles of the initial residual stresses in the longitudinal and the transversal directions, respectively
$\sigma_{Rxx}(0)$, $\sigma_{Ryy}(0)$	initial surface residual stresses in the longitudinal and the transversal directions, respectively
$\sigma^*_{Rxx}(z)$, $\sigma^*_{Ryy}(z)$	in-depth profiles of the stabilized residual stresses in the longitudinal and the transversal directions, respectively
$\sigma^*_{Rxx}(0)$, $\sigma^*_{Ryy}(0)$	stabilized surface residual stresses in the longitudinal and the transversal directions, respectively
τ^a	amplitude of the Tresca shear stress
λ	wavelength of the X-ray
θ	angle that the incident beam makes with the diffracting plane (so-called the Bragg angle)
ψ	angle between the normal of the sample and the normal of the diffracting plane (bisecting the incident and diffracted beams)
ϕ	angle between a fixed direction in the plane of the sample and the projection in that plane of the normal of the diffracting plane

stresses on the high cycle fatigue (HCF) behaviour can be predicted using a multiaxial fatigue criterion such as the Dang Van's criterion [16,18–24]. In this case, it is necessary to evaluate the stabilized state of residual stresses under cyclic loading. In order to reach this target, many empirical models were developed from experimental results [25–30]. However, these models are simples and can't take into account of all the influence parameters with an acceptable accuracy. For this reason, it's important to use numerical approach based on the FE method. Indeed, the proposed FE models [20,21,25,31–34] have the advantage to simulate the cyclic hardening behaviour of the surface layers which represents the main phenomenon of residual stress relaxation. However, the implementation of these models presents the difficulty to identify the cyclic hardening law and the calibration of its material constants [20,32].

Several material models are usually used to analyze the mechanical relaxation of residual stresses at the surface layer. Smith et al. [32] have analyzed, using FE simulations, the interaction between residual stresses and cyclic mechanical loading in the case of forged and shot-blasted bars of En 15R. The initial residual stress distribution and the initial state of the material model are introduced in the FE model. It was found that the results of residual stress simulations depend on the type of model material. The simple linear model always leads to residual stress relaxation only in the first cycle. In contrast, the multilinear model demonstrates continuous relaxation with increasing number of cycles. The extent of relaxation is also greater using the multilinear model compared to the linear model. Zhuang and Halford [25] proposed a physics relaxation model based on two important ingredients: (i) the degree of cold-working for each surface layer characterized by a local material yield strength, and (ii) an accurate material stress–strain response under cyclic loading. This model has been tested in the case of wrought IN718 rectangular bars treated by shot peening, laser shot peening and low plasticity burnishing. A nonlinear isotropic/kinematic hardening model was employed in the FE model. The results of simulations predict the effect of three dominant relaxation parameters, load amplitude, load ratio and degree of initial cold-working.

On the other hand there is few works which predict the residual stress relaxation and its influence on the HCF behavior of metallic parts and structures. Bertini et al. [33] discussed the influence of the ageing and shot peening treatments on the HCF behavior (10^6 cycles or more) of Al-alloy welded joints, with the aid of a FE model taking into account of residual stress relaxation. The material behaviour was represented by a bilinear kinematic hardening model. The results of calculations confirmed that the zone undergoing plastic strain was very small, as compared to the specimen thickness. Moreover, an elastic shakedown was predicted after the first cycle, with no cyclic plasticity. This permitted to predict with acceptable approximation the fatigue limits using the Gerber's uniaxial criterion. Boyce et al. [34] evaluated numerically (FE analysis) and experimentally (synchrotron X-ray diffraction) the fatigue loading-induced relaxation of localized residual stresses formed around a site of simulated foreign object damage in a forged Ti–6Al–4V alloy. A nonlinear isotropic/kinematic hardening material model was used in the FE analysis. The relaxed residual stress state, combined with the product of the applied stress and an appropriate stress-concentration factor at the damage site, provides a means to estimate the driving forces and also the sites for crack nucleation under different HCF loadings.

The objective of this work is to evaluate experimentally and numerically the residual stress relaxation and its effect on bending fatigue limits of AISI 316L steel ground surfaces in comparison with electro-polished surfaces.

2. Material and experimental procedure

2.1. Material

The material studied is an AISI 316L austenitic stainless steel according to the ASTM standard. It was received in the form of cylindrical bars of diameter 20 mm. The chemical composition of this material is (wt.%): Fe–0.02C–0.56Si–1.67Mn–0.041P–0.041S–17.24Cr–11.14Ni–1.96Mo–0.066N–0.35Cu–0.055V. The main mechanical properties after an annealing treatment (cooling in air after heating for 1 h at 1050 °C) are: E(GPa) = 196, $\sigma_{Y0.2}$(MPa) = 220, σ_{UTS}(MPa) = 600, σ_F(MPa) = 400, $T.E.$(%) = 80, $HV_{0.1}$ = 190. The micro-structure of the material is composed of austenitic grains with an average size of 60 μm (Fig. 1).

2.2. Surface finishing conditions

A notched specimen ($K_t \approx 1.6$) devoted to plane bending fatigue tests was selected for the purpose of this study (Fig. 2a). Two sets of specimens were machined by milling and next were treated together by annealing under the same conditions presented above. Finally, the two sets of specimens were differently finished by grinding and electropolishing operations using the following conditions:

(i) Grinding conditions: The notches of a first set of 20 specimens were ground simultaneously using a V-shaped grinding wheel and a fixture device on the grinding machine. In the beginning, several passes with gentle conditions (a depth of cut of 5 μm and a work speed of 4 m/min) were carried until the wheel touches all the notches of specimens. Finally, the notches were finished using a final pass under the conditions given in Table 1.

(ii) Electropolishing conditions: This treatment was applied to a second set of 26 specimens. The surface of each specimen was completely prepared by electrolytic polishing operations in order to obtain very smooth and virgin surfaces. The device used is composed of the following elements: a stainless steel container (cathode) containing a chemical solution (phosphoric acid + glycerol + water), the specimen (anode), a DC generator and two conductor cables. The operating conditions which were applied to dissolve a thin layer of approximately 50 μm are: a voltage of 10 V, a current of 5 A and a time of about 20 min.

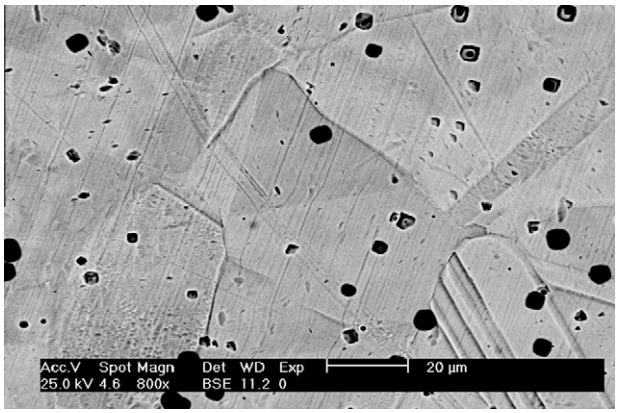

Fig. 1. Austenitic structure of the AISI 316L steel.

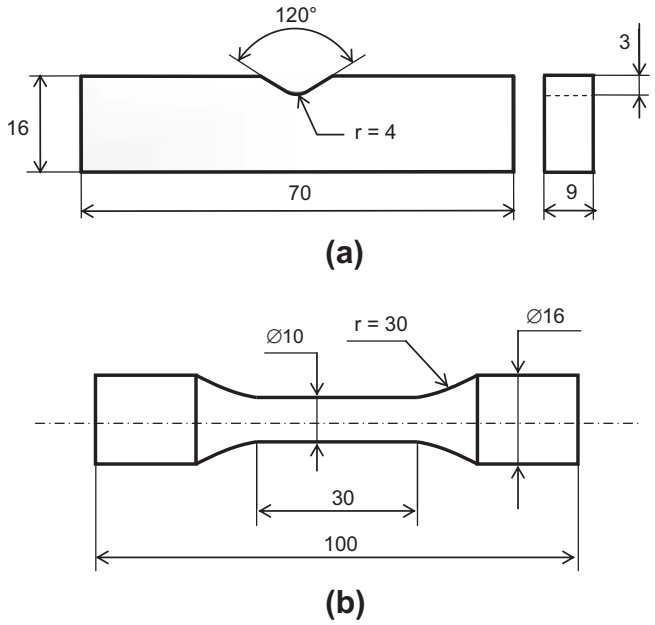

Fig. 2. Geometry and dimensions (in mm) of two fatigue specimens: (a) notched specimen ($K_t \approx 1.6$) used in HCF tests under both 3-point and 4-point bending configurations and (b) smooth specimens used in LCF tests under reversed tension–compression.

2.3. Testing methods

2.3.1. Characterization of the surface properties

The micro-structure of both ground and electro-polished surfaces was characterized by Vickers micro-hardness filiations under a load of 100 g ($HV_{0.1}$) using a SHIMADZU HMV-2000 micro-hardness tester. The measurements were performed on one side of the specimen and close to the notch root.

The initial and stabilized residual stress fields were determined using the X-ray diffraction method [35,36]. In this study, the XRD residual stress measurements were carried out at the middle of the notch root using a PROTO-iXRD diffractometer. The experimental conditions for determining of residual stresses in the two preferred measurement directions (longitudinal and transversal directions) are given in Table 2. The in-depth residual stresses were measured through successive electropolishing of a restricted area of about 2 mm at the notch root. The layers removal was controlled by a digital comparator with precision of 1 μm.

The ground surface roughness was measured using a PERTHOMETER-S3P profilometer. The surface roughness profiles were recorded on one flat surface of the notch, following the perpendicular direction to the grinding streaks. The parameters R_a and R_t were selected to quantify the surface roughness.

The texture and the eventual defects of the ground surface were examined before fatigue testing at the notch root using a scanning electron microscope (SEM).

2.3.2. Fatigue tests and damage mechanisms

The ground and electro-polished specimens were submitted to high cycle bending fatigue tests using various conditions. These tests were performed on an MTS-810 servo-hydraulic material-testing machine by applying controlled loads with 30 Hz frequency and for a censure of 2×10^6 cycles. The fatigue limits at 2×10^6 cycles with 50% failure probability were estimated by applying the staircase method [37,38]. The electro-polished specimens were subjected to 4-point plane bending fatigue tests with two different load ratios, $R_\sigma = 0.1$ and $R_\sigma = 0.3$, in order to determine two fatigue limits of the base metal. Fig. 3a and b shows the two plane bending

Table 1
Grinding conditions.

Grinding wheel	99A46H7VNE with V shape
Grinding mode	Down grinding
Wheel speed, v_s (m/s)	22
Work speed, v_w (m/min)	8
Depth of cut, a_e (μm)	10
Refrigerant fluid	Soluble oil: 20% smilax-89 + 80% water (7.2 L/min)
Workpiece material	AISI 316L (EN X2CrNiMo17-12-2)

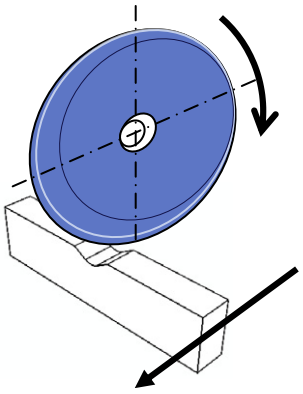

Table 2
X-ray diffraction parameters.

Radiation	Cr Kα*x* λ 0.2102 nm
Current (mA)	5
Voltage (kV)	20
Acquisition device	ψ
Young's modulus (MPa)	196,000
Poisson's modulus	0.29
X-ray diffraction planes	$(311)_\gamma$, $2\theta \approx 152{,}3°$
Beam diameter (mm)	2
ψ oscillation (°)	±3
Number of ψ	11
φ angles (°)	0 and 90

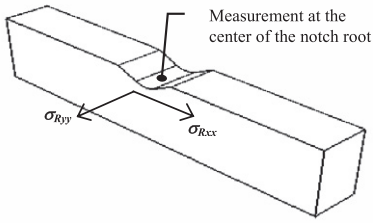

configurations and the devise used for the 4-point bending fatigue test. The ground specimens were subjected to 3-point and 4-point plane bending fatigue tests with only one load ratio $R_\sigma = 0.1$. This choice is intended to study the influence of the bending mode on the residual stress relaxation and the fatigue limit of the AISI 316L steel ground specimens.

The role of the surface quality in the initiation and propagation of fatigue cracks was clarified by SEM examinations. The stabilized residual stress profiles were measured at the notch root of an unbroken specimen after 2×10^6 cycles close to the fatigue limit.

3. Results

3.1. Initial surface quality

3.1.1. Surface microgeometrical quality

Fig. 4 is an SEM micrograph of the ground surface. It reveals a typical texture characterized by machining grooves and a distribution of folds and scales inherent to the grinding process and the material ductility. It should be noted that the surface is totally exempt of thermal cracks. The mean values of the principal roughness parameters are: $R_a = 1.5$ μm and $R_t = 11.7$ μm.

3.1.2. Surface work-hardening

The micro-hardness profile of the electro-polished surface (Fig. 5) has been established over a surface layer of 300 μm. It can be seen that the electropolished surface has nearly the same micro-hardness value than the base material ($HV_{0.1} \approx 190$).

The micro-hardness profile measured in-depth of the ground surface (Fig. 5) shows that the grinding induces a high hardening gradient over a superficial layer of ≈100 μm. The surface is characterized by a maximum hardening rate of ≈80% with respect to the base material.

3.1.3. Initial residual stresses profiles

The measures in the longitudinal direction ($\phi = 0°$) allows to determine the stresses $\sigma_{Rxx}(z)$ and $\tau_{Rxz}(z)$ while the measures in the transversal direction ($\phi = 90°$) determine the stresses $\sigma_{Ryy}(z)$ and $\tau_{Ryz}(z)$. However, the results of measurements in both direc-

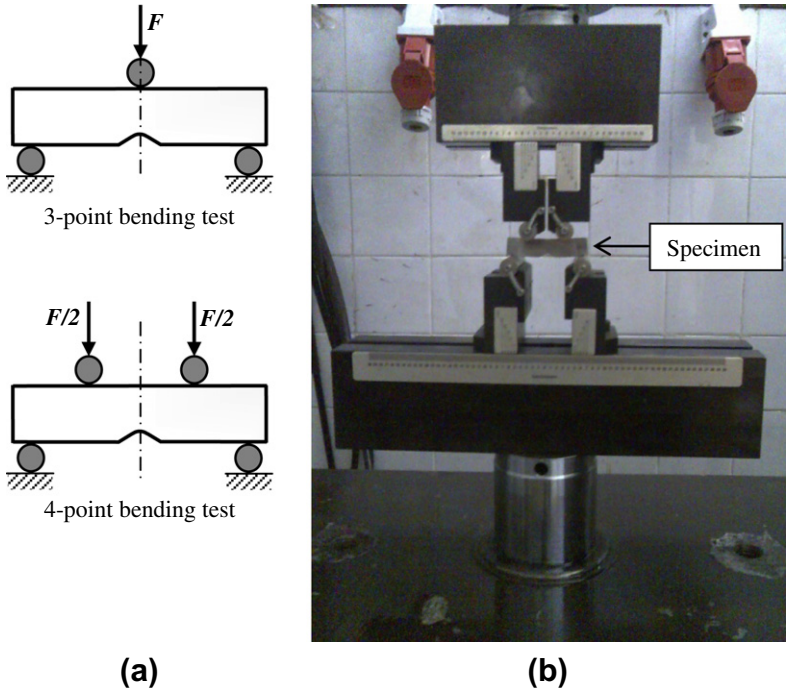

Fig. 3. (a) Two plane bending configurations and (b) devise of 4-point plane-bending fatigue test.

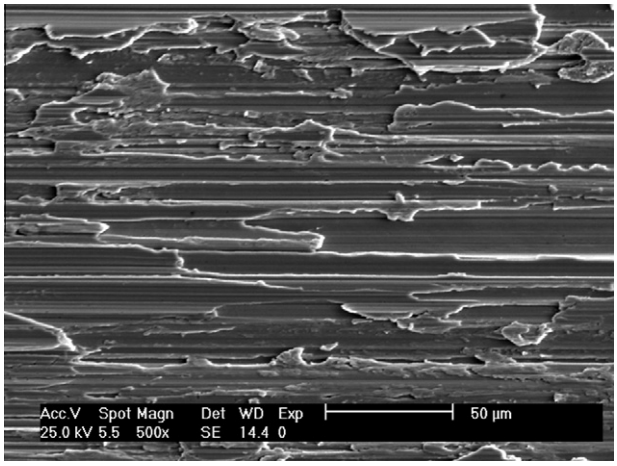

Fig. 4. Texture of the AISI 316L steel ground surface.

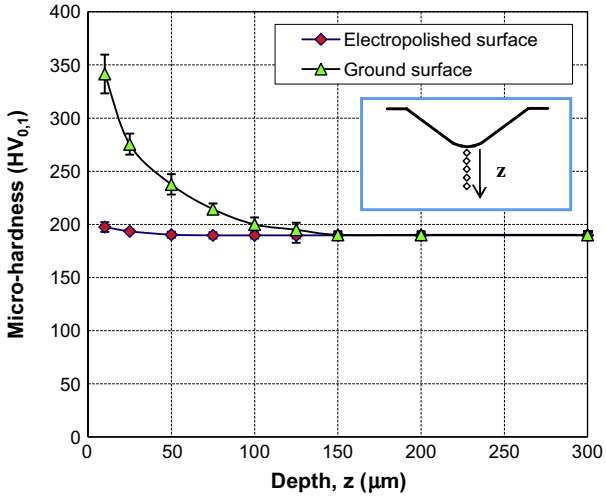

Fig. 5. Micro-hardness profiles in-depth of the electro-polished and ground surfaces.

tions show that shear stress values can be considered negligible in comparison with the normal stress values.

Fig. 6a shows that the electro-polished surface is subjected to tensile residual stresses over a layer of 80 µm. These stresses present low values which don't exceed approximately 80 MPa in both measurement directions. On the other hand, Fig. 6b shows that the ground surface is characterized by high tensile residual stress profiles, particularly in the transversal direction (parallel to grinding grooves). The maximum values of stresses are situated at the surface: $\sigma_{Rxx}(0) = 510$ MPa and $\sigma_{Ryy}(0) = 765$ MPa.

3.2. Fatigue results

Fig. 7 shows the *S–N* diagram (nominal stress range versus the number of cycles) for the electropolished and ground surfaces subjected to various fatigue test conditions. The determined fatigue limits ($\Delta\sigma_D$) are summarized in Table 3. It was found that the 4-point bending fatigue limit of the electropolished specimens decreases of about −17% when the loading ratio increases from $R_\sigma = 0.1$ to $R_\sigma = 0.3$. On the other hand, the grinding treatment provokes a significant degradation of −35% for the 4-point bending fatigue limit comparatively to that of the electropolished surface. However, the 3-point bending fatigue limit of the ground surface is greater of about 50% comparatively to the 4-point bending fatigue limit of the same surface.

All the broken specimens at electopolished or ground state are characterized by a transversal fracture which occurs systematically at the notch root. An SEM micrograph at the fracture surface of a ground specimen shows that the cracks nucleate at the surface and they are related to the machining grooves (Fig. 8).

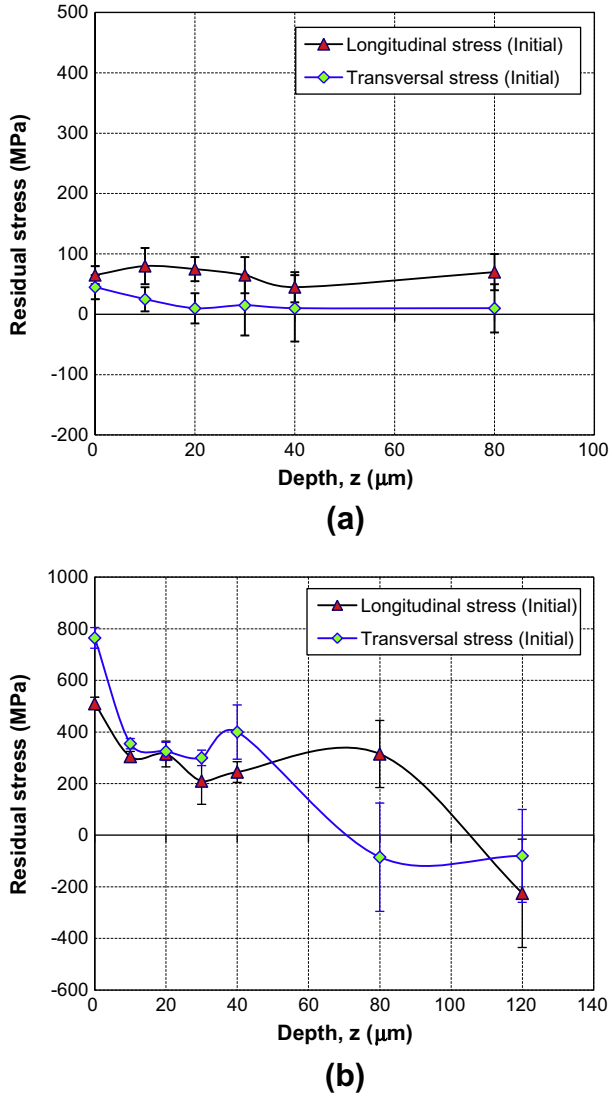

Fig. 6. Initial residual stress profiles: (a) after electro-polishing and (b) after grinding.

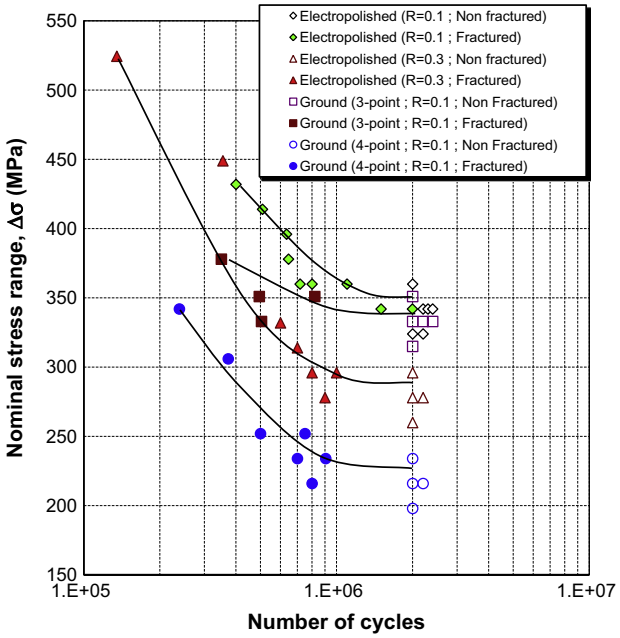

Fig. 7. SN diagram.

Table 3
Principal results of HCF tests.

Surface state	Bending mode	R_σ	$\Delta\sigma_D$ (MPa)	Percentage of change (%)[a]
Electro-polished	4-point	0.1	350	0
	4-point	0.3	290	−17
Ground	4-point	0.1	230	−35
	3-point	0.1	343	−2

[a] The 4-point bending fatigue limit ($R_\sigma = 0.1$) of the electropolished specimens is considered as reference.

3.3. Residual stress relaxation

Fig. 9 shows the stabilized residual stress profiles measured in electropolished specimens which have supported 2×10^6 cycles near the two fatigue limits at $R_\sigma = 0.1$ and $R_\sigma = 0.3$. They reveal in the two cases, compressive residual stresses in the longitudinal direction acting over a surface layer of 80 μm (Fig. 9a). The surface longitudinal stress under the load $R_\sigma = 0.1$ is higher ($\sigma^*_{Rxx}(0) \approx -140$ MPa) than that under the load $R_\sigma = 0.3$ ($\sigma^*_{Rxx}(0) \approx -50$ MPa). The surface transversal stresses are tensile stresses characterized by almost the same level ($\sigma^*_{Ryy}(0) \approx +145$ MPa) for both loading ratios (Fig. 9b). In sub-layer, for $z = 30$ μm, the transversal stress level increases substantially under the load ratio $R_\sigma = 0.3$ ($\sigma^*_{Ryy}(30) \approx +280$ MPa) with respect to the load ratio $R_\sigma = 0.1$ ($\sigma^*_{Ryy}(30) \approx +150$ MPa).

Fig. 10a and b shows the stabilized residual stress profiles measured in ground surfaces which have supported 2×10^6 cycles near the 3-point and 4-point bending fatigue limits ($R_\sigma = 0.1$). For the 3-point bending test, the initial residual stresses are completely relaxed at the surface ($\sigma^*_{Rxx}(0) \approx 0$ MPa and $\sigma^*_{Ryy}(0) \approx 0$ MPa). The subsurface stresses are compressive and characterized by maximum absolute values in depth of 40 μm: $\sigma^*_{Rxx}(0) \approx -115$ MPa and $\sigma^*_{Ryy}(0) \approx -225$ MPa. For the 4-point bending test, the initial residual stresses were partially relaxed and remain tensile stresses in both measurement directions. This relaxation is very slight at the surface leading to the following stabilized values: $\sigma^*_{Rxx}(0) \approx 420$ MPa and $\sigma^*_{Ryy}(0) \approx 710$ MPa.

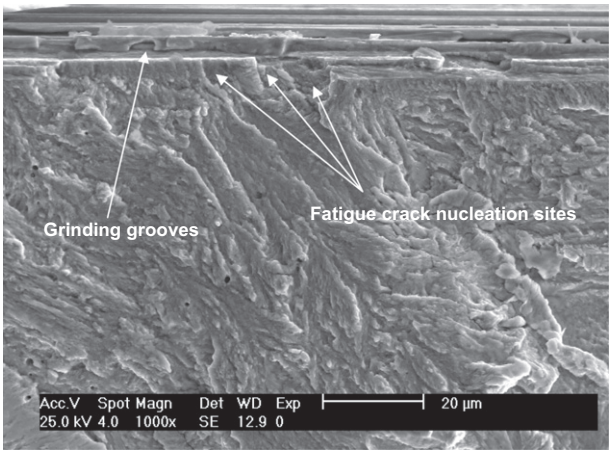

Fig. 8. SEM micrograph of the fracture surface of a ground specimen.

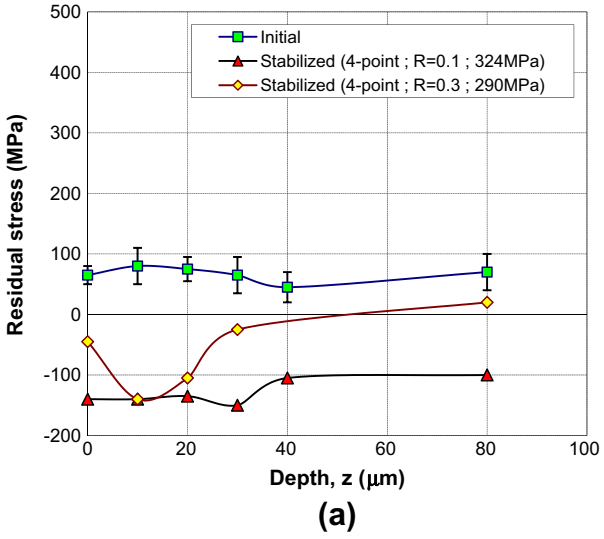

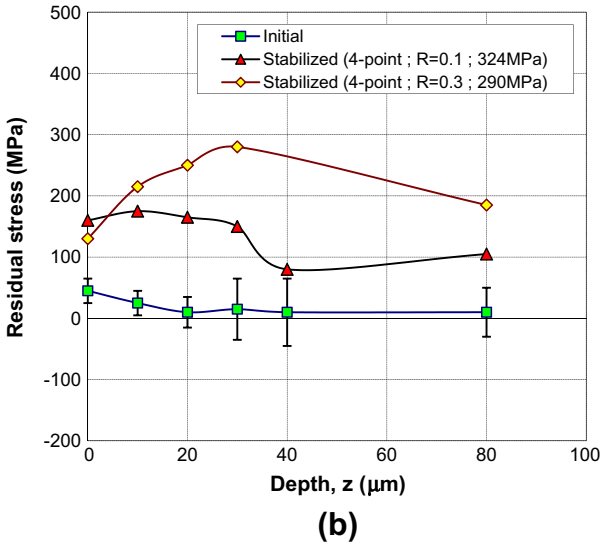

Fig. 9. Stabilized residual stress profiles of the electro-polished surface after 4-point bending fatigue tests near fatigue limits: (a) longitudinal stresses (σ_{Rxx}) and (b) transversal stresses (σ_{Ryy}).

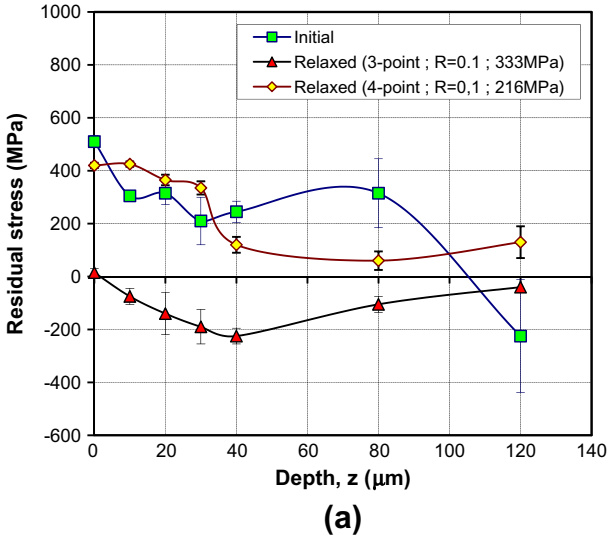

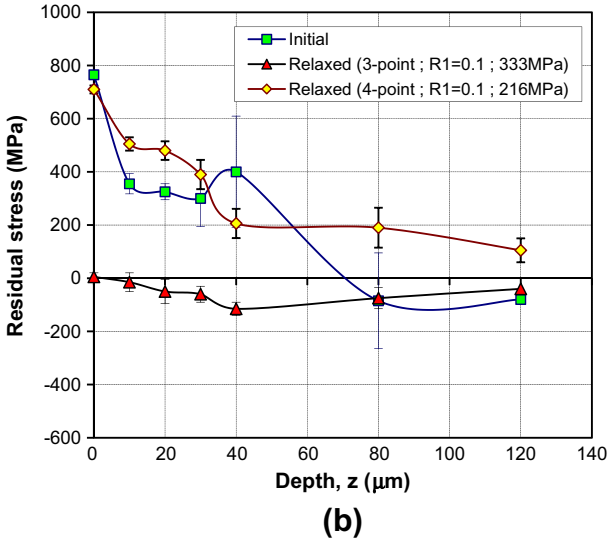

Fig. 10. Stabilized residual stress profiles of the ground surface after 3-point and 4-point fatigue tests near fatigue limits: (a) longitudinal stresses (σ_{Rxx}) and (b) transversal stresses (σ_{Ryy}).

4. FE analysis of residual stress relaxation

The FE method was applied using the computer code ABAQUS/Standard (version 6.5) [39] in order to simulate the residual stress relaxation acting at the notch root of the ground specimen under both 3-point and 4-point bending tests. The total cyclic stress tensor, expressed by Eq. (1), was also evaluated for each fatigue limit.

$$\underline{\underline{\sigma}}_t(z,t) = \underline{\underline{\sigma}}_{app}(z,t) + \underline{\underline{\sigma}}^*_R(z) \quad (1)$$

4.1. Geometry and meshing

The analysis of the residual stress relaxation under 3-point and 4-point bending tests was carried out using two FE models. Both bending tests present symmetry plane (O, X, Z) at the middle thickness (Fig. 11). The specimen thickness which equal to 9 mm cannot be considered negligent in comparison with the width which equal to 13 mm. Therefore, the FE models are considered in two dimensions (2D) and based on the hypothesis of plane strain. In addition, since each bending configuration has a symmetry plane (O, Y, Z) at the middle length, only the half of the specimen was considered. The geometry of each FE model (Fig. 11) was meshed by CPE3 type triangular elements (9529 elements and 18,555 nodes). The meshing of the grinding affected layer (thickness of 100 µm) was performed with finer elements of 10 µm size.

4.2. Cyclic hardening model for the base material

The cyclic behavior of the AISI 316L steel was experimentally determined by low-cycle fatigue (LCF) tests with controlled strain in reversed tension–compression ($R_\varepsilon = -1$). The tests were performed using an MTS-810 servo-hydraulic machine on a set of electropolished cylindrical specimens with diameter of 10 mm (Fig. 2b). The total strain amplitude of the cyclic loading were applied with four values: $\Delta\varepsilon_t/2$ (%) = 0.3, 0.5, 0.7 and 1 which are controlled by means of a longitudinal extensometer. The hysteresis loops for the different imposed strain amplitudes were used to determine the cyclic hardening curves which show the evolution of the stress amplitude (σ_a) versus the number of cycles (Fig. 12). These curves show three common phases for austenitic stainless steels subjected to moderate strain amplitude (less than 0.8%) [40,41].

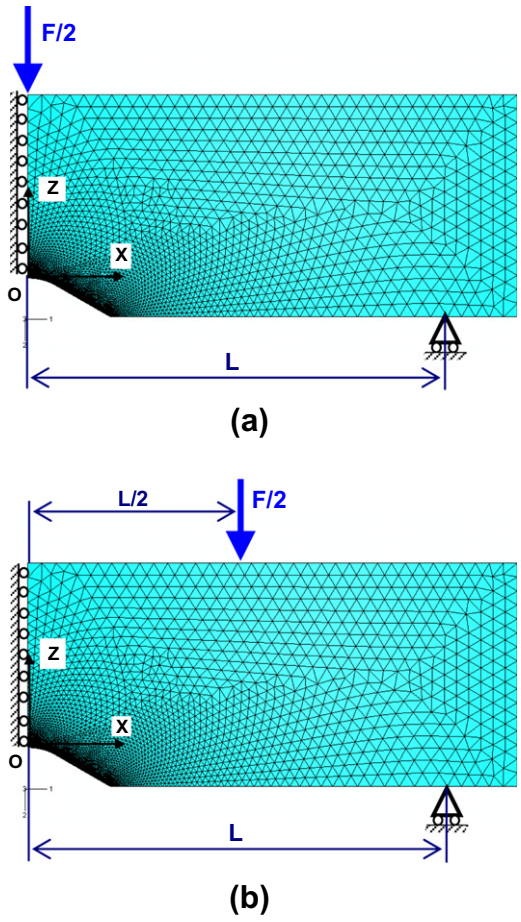

Fig. 11. Geometry and meshing of 2D FE models: (a) model for the 3-point bending test and (b) model for the 4-point bending test.

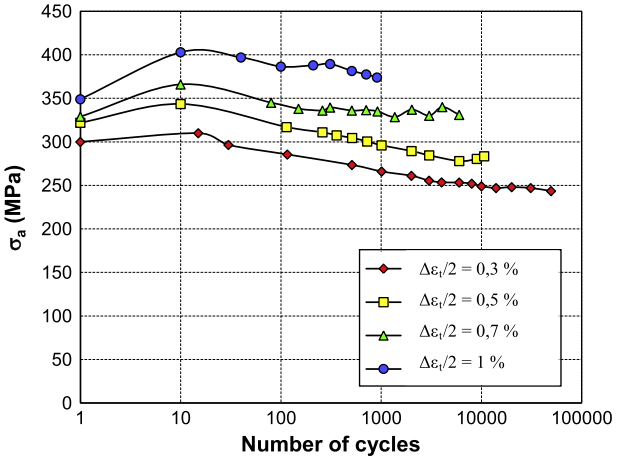

Fig. 12. Evolution of the stress amplitude versus the number of cycles for the AISI 316L steel.

(i) A first hardening phase during the first cycles (from 1 to 10 cycles), more important that the amplitude of plastic deformation is higher.
(ii) A second phase of quasi-stabilization (more than 10 cycles) intervening earlier that the imposed strain amplitude is higher.
(iii) The test finishes with a fall of the stress amplitude due to the rapid development of fatigue cracks leading to the fracture of the specimen.

In this study, the quasi-stabilization phase is chosen as a steady state for modelling the cyclic elasto-plastic behaviour of the base material. As shown in Fig. 13, the steady state described above is characterized by two phenomena of hardening: an isotropic hardening combined with a nonlinear kinematic hardening. This last allows transposing the Bauschinger effect. Consequently, we adopt the isotropic and nonlinear kinematic hardening model proposed by Chaboche [42]. This model is able to take into account various phenomena such as ratcheting, relaxation of the mean stress, and cyclic hardening that are typical of materials subjected to cyclic loading. In this model, the yield criterion of Von Mises, the plastic flow law and the two hardening variables, $\underline{\underline{X}}$ and R, are defined as follows:

$$f = J_2(\underline{\underline{\sigma}} - \underline{\underline{X}}) - R - k \leqslant 0 \tag{2}$$

$$d\underline{\underline{\varepsilon}}^p = d\lambda \frac{\delta f}{\delta \underline{\underline{\sigma}}} \tag{3}$$

$$d\underline{\underline{X}} = \frac{2}{3} C d\underline{\underline{\varepsilon}}^p - \gamma \underline{\underline{X}} dp \tag{4}$$

$$dR = b(Q - R)dp \tag{5}$$

where $dp = \sqrt{(2/3)d\underline{\underline{\varepsilon}}^p : d\underline{\underline{\varepsilon}}^p}$ indicates the increment of the equivalent plastic strain. $\underline{\underline{X}}$ and R are the centre and the size of the load surface, respectively. The base material constants k, C, γ, Q and b of this model for the 316L stainless steel were identified according to the method given in Ref. [42] and using the results of LCF tests presented above. The obtained values are summarized in Table 4. To verify the capability of the material model, the cyclic stress response at strain amplitude of 0.3% was compared with that of the constitutive model. The results show that the shape of the hysteresis loop is successfully described by the model as shown in Fig. 14. So, this model is employed to estimate the relaxation of residual stress at the notch root of ground specimens subjected to 3-point and 4-point bending tests.

4.3. Introduction of initial surface properties

Under the code ABAQUS, the grinding residual stresses were introduced in the FE models as an initial condition using a subroutine written in FORTRAN language [39]. These stresses were then equilibrated in a first STEP of calculation. The hardening of each layer of 10 µm was taken into account following the method proposed in Ref. [32] to ensure steady-state of initial residual stresses.

4.4. Results of FE analysis

The FE simulation of grinding residual stress relaxation was performed by applying a cyclic loading corresponding to the fatigue limit under 3-point or 4-point bending test. The number of cycles must lead to numerical values of the stabilized residual stresses close to the experimental values. This is obtained by calibration of the material constants of the cyclic hardening law for the ground layer under both bending modes. The new values of these constants are given in Table 4.

Figs. 15 and 16 compare the profiles of stabilized residual stresses obtained experimentally with those simulated numerically for the 3-point and 4-points bending tests, respectively. In the case of the 3-point bending test (Fig. 15), the numerical and experimental profiles of stabilized residual stresses present almost the same form. The relaxed longitudinal stresses in the first 20 µm are slightly underestimated by the calculation, a maximum deviation of about 80 MPa recorded at surface (Fig. 15a). However, the relaxed transversal stresses are overestimated by the calculation,

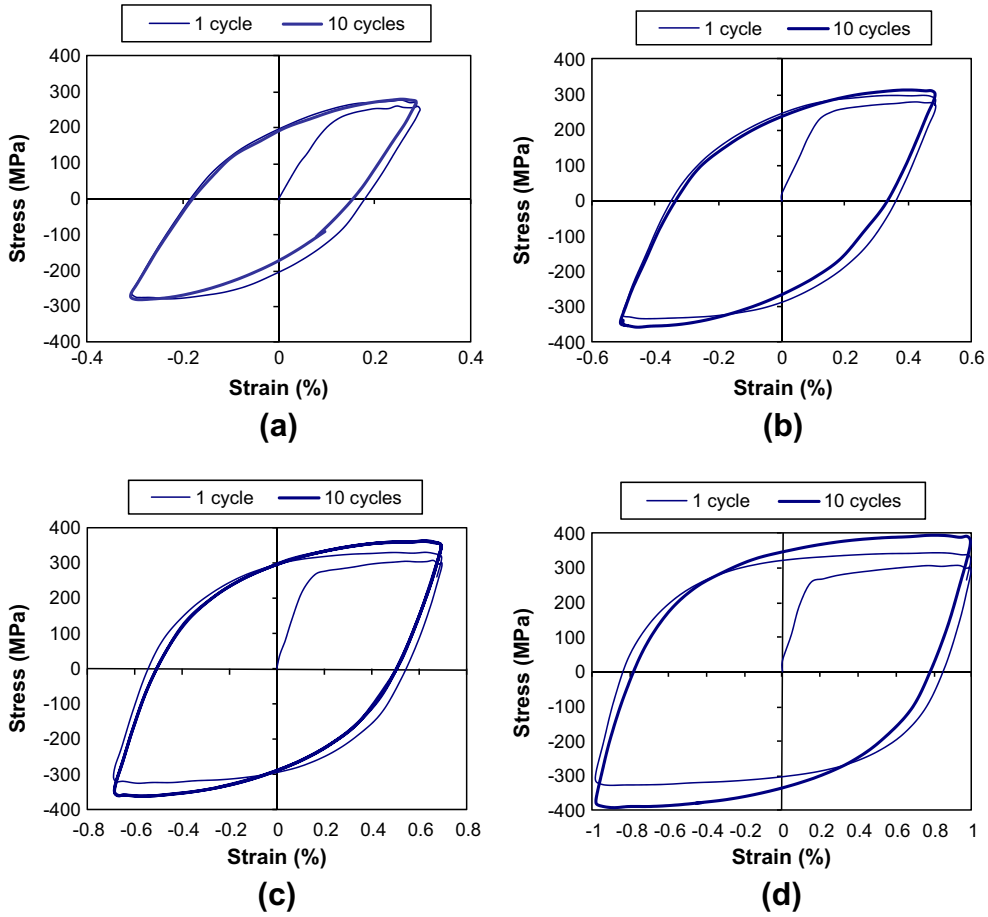

Fig. 13. Steady loops of the strain–stress law of the AISI 316L steel under strain-controlled tests ($R_\varepsilon = -1$) with several strain amplitudes: (a) $\Delta\varepsilon t/2 = 0.3\%$, (b) $\Delta\varepsilon t/2 = 0.5\%$, (c) $\Delta\varepsilon t/2 = 0.7\%$, and (d) $\Delta\varepsilon t/2 = 1.0\%$.

Table 4
Constants of the cyclic hardening law for the AISI 316L steel with different states and under different cyclic loading conditions.

Material state	Cyclic loading conditions	E (GPa)	ν	k (MPa)	C (MPa)	γ	Q (MPa)	b
Base material	Reverse tension–compression ($R_\varepsilon = -1$)	196	0.29	220	30,000	60	150	1
Ground	3-Point bending ($R_\sigma = 0.1$)	196	0.29	220	70,000	40	150	4
	4-Point bending ($R_\sigma = 0.1$)	196	0.29	220	150,000	20	150	4

especially at surface for which the difference is about of +150 MPa compared with the experimental result (Fig. 15b). For the 4-point bending test (Fig. 16), the numerical and experimental profiles have almost the same form. However, the values of stabilized residual stresses are underestimated by the calculation for both longitudinal and transverse directions. The difference is lower at the surface, not exceeding 100 MPa.

5. Discussion

5.1. Initial residual stress

The results of the initial residual stress profiles show maximum values of $\sigma_{Rxx}(0) = 510\ MPa$ and $\sigma_{Ryy}(0) = 765\ MPa$ at the surface. The Von Mises's equivalent stress corresponding to these stresses is given by Eq. (6). Its value ($\sigma_R^{VM}(0) = 675$ MPa) is considerably higher than the yield stress ($\sigma_{Y0.2} = 220$ MPa) of the base material and exceeds slightly its ultimate tensile stress ($\sigma_{UTS} = 600$ MPa). This remark can be explained by the surface hardening induced by grinding. This change is responsible of the generation of initial residual stresses. It is characterized by an important increase of hardening which equals approximately to 80% with respect to the base material. Consequently, the grinding residual stresses operate in an elastic domain having a yield stress ($\sigma_{Y0.2}$) higher than that of the base material.

$$\sigma_R^{VM}(0) = \frac{1}{\sqrt{2}}\sqrt{(\sigma_{Rxx}(0))^2 + (\sigma_{Ryy}(0))^2 + (\sigma_{Rxx}(0) - \sigma_{Ryy}(0))^2} \qquad (6)$$

5.2. Residual stress relaxation

For the electro-polished surface, the evolution of residual stresses under 4-point bending tests with two different loading ratios ($R_\sigma = 0.1$ and $R_\sigma = 0.3$) can be explained by the creating of cyclic plastic strain at the notch root of specimens [13,27]. Indeed, the FE analyses demonstrate that the maximum value of Von Mises stress corresponding to each fatigue limit exceeds the tensile yield strength of the base material ($\sigma_{Y0.2} = 220$ MPa). The compressive stresses which appear in the longitudinal direction are due to a

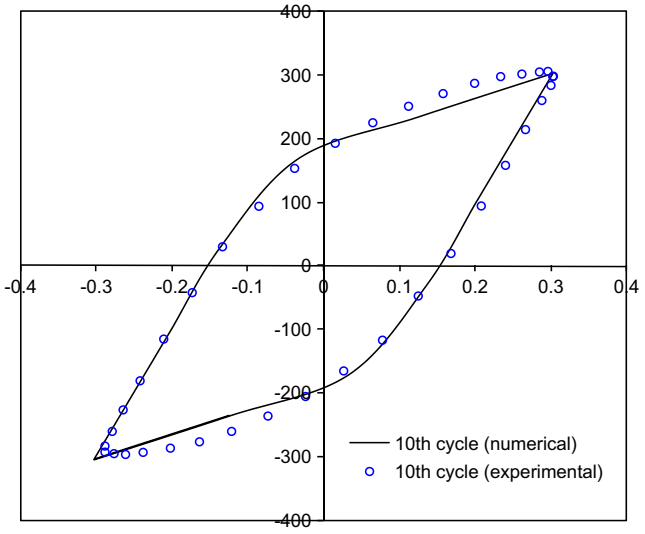

Fig. 14. Predicted hysteresis loop after 10 cycles under the 0.3% strain amplitude test.

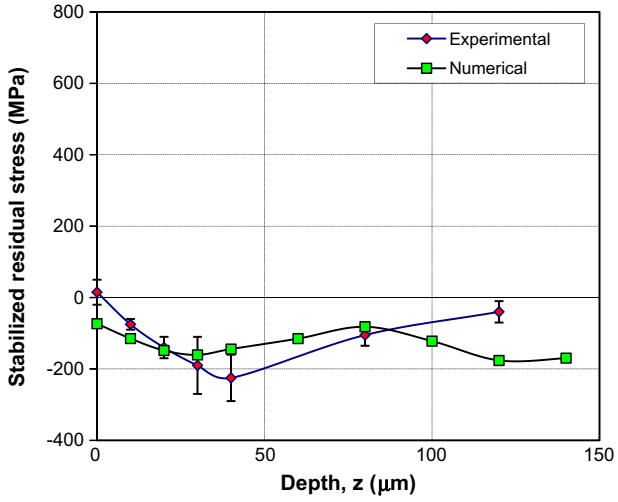

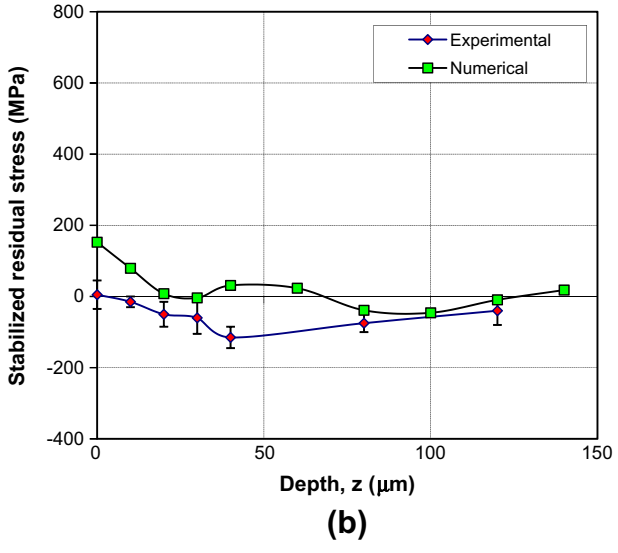

Fig. 15. Comparison between numerical and experimental profiles of stabilized residual stresses under 3-point bending test: (a) longitudinal stresses (σ_{Rxx}) and (b) transversal stresses (σ_{Ryy}).

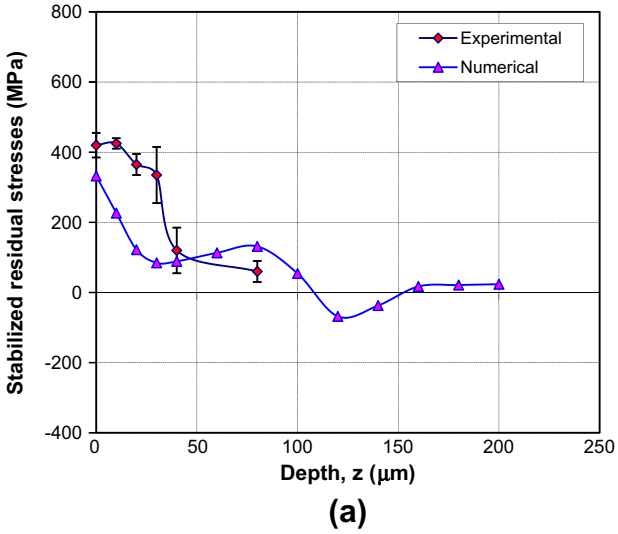

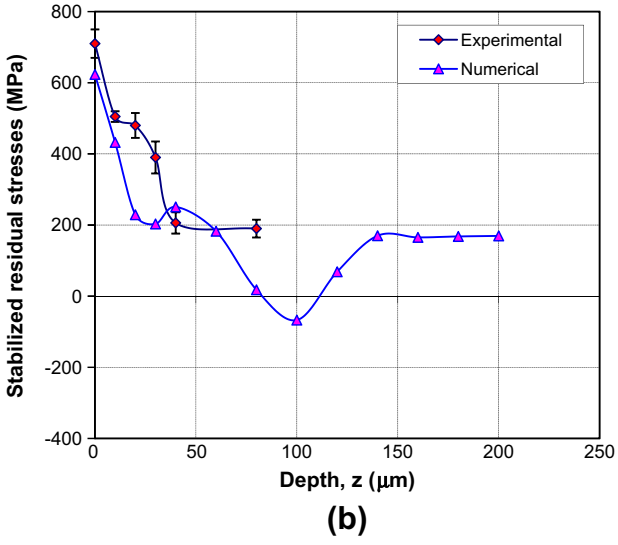

Fig. 16. Comparison between numerical and experimental profiles of stabilized residual stresses under 4-point bending test: (a) longitudinal stresses (σ_{Rxx}) and (b) transversal stresses (σ_{Ryy}).

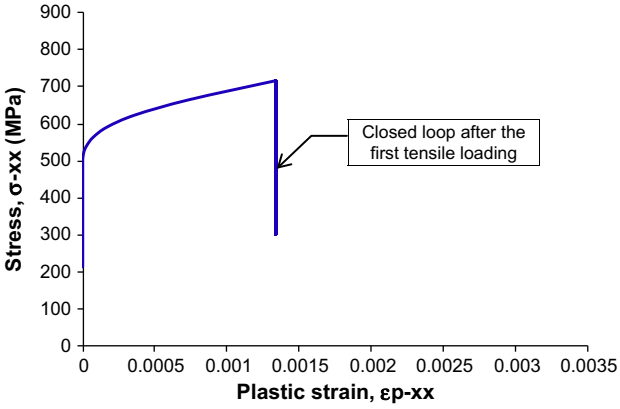

Fig. 17. The stress/plastic-strain relationship at the notch root of ground specimens subjected to 4-point bending test at the fatigue limit (showing an elastic shakedown after the first loading).

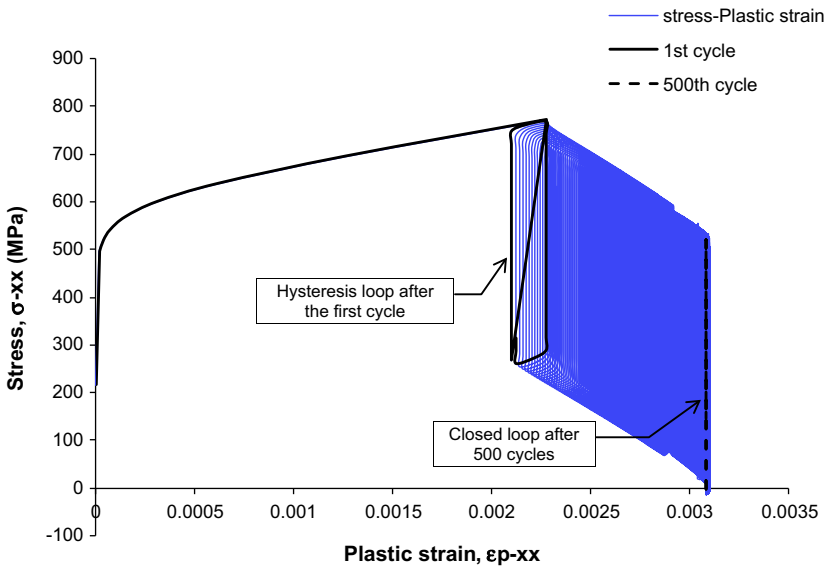

Fig. 18. The stress/plastic-strain relationship at the notch root of ground specimens subjected to 3-point bending test at the fatigue limit (showing an elastic shakedown after nearly 500 cycles).

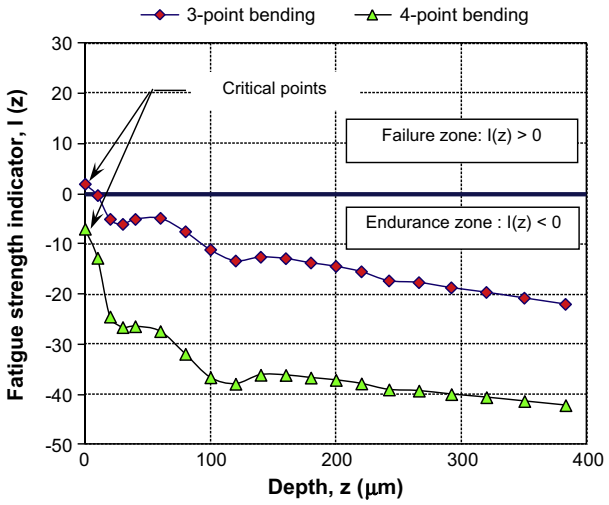

Fig. 19. Fatigue strength indicator profiles for the AISI 316L steel ground specimens under 3-point and 4-point bending fatigue tests.

plastic elongation, while the tensile stresses appearing in the transversal direction are due to a plastic shortening.

In the case of ground surface, the initial residual stresses were slightly relaxed under the 4-point bending test near the fatigue limit ($\Delta\sigma_D$ = 230 MPa). The FE analyses show that the cyclic loading induces a low value of the equivalent plastic strain at the notch root of specimens ($\varepsilon^p_{eq} \approx 0.0019$). In addition, the plastic deformation is occurred only after the first loading cycle (Fig. 17), and thereafter the material cyclic behaviour corresponds to an elastic-shakedown response. This explains the partial relaxation of residual stresses which remain tensile stresses near the fatigue limit, as shown in Fig. 10. On the contrary, under the 3-point bending fatigue test near the fatigue limit ($\Delta\sigma_D$ = 343 MPa), the grinding residual stresses are completely relaxed at the notch root (Fig. 10). The FE analyses show that this beneficial effect is due to a larger accumulation of the local plastic strain ($\varepsilon^p_{eq} \approx 0.03$) than in the case of 4-point bending test. Fig. 18 shows that the cyclic behaviour of the notch root is characterized by a gradual plastic shakedown with hysteresis loops. During the shakedown process both cyclic ratcheting and mean stress relaxation occur simultaneously with decease rate. This process tends after almost 500 cycles to an elastic-shakedown response with closed loop (i.e. no further plastic deformation). Therefore, the grinding residual stresses reach a stabilized state.

Consequently, the FE analyses demonstrate that the residual stress relaxation depends strongly on the plastic strain evolution under cyclic loading. Indeed, greater is the plastic strain accumulation higher is the residual stress relaxation [12,13]. On the other hand, the difference of residual stress relaxation between the 3-point and 4-point bending tests can be attributed to the stress concentration effect which is characterized by two different values of the stress concentration factor: $K_{t\text{-}3p}$ = 1.54 and $K_{t\text{-}4p}$ = 1.66. This effect changes the cyclic hardening behavior of the notch root as has been demonstrated previously.

5.3. Influence of stabilized residual stresses on fatigue strength

For the electropolished condition, the results of fatigue bending 4-point tests with two different loading ratios have showed that the fatigue limit of the AISI 316L steel decreases with increasing of load ratio from R_σ = 0.1 to R_σ = 0.3. This result is in good agreement with the effect of mean stress on the amplitude of the fatigue limit [2]. It should be noted here that the stabilized residual stresses seem not influence the two fatigue limits of the electropolished material. This can be justified by the fact that the compressive stresses in the longitudinal direction are almost offset by the tensile stresses in the transversal direction over a surface layer of 20 μm.

The fatigue strength of AISI 316L steel is significantly influenced by the grinding treatment which leads to a significant degradation of the 4-point bending fatigue limit estimated at ≈−35% in comparison with the electropolished surface. This degradation is accompanied by a slight relaxation of the grinding residual stresses which remain with tensile values at the surface and which play a detrimental effect on fatigue strength [10]. On the other hand, the fatigue limit of the AISI 316L steel ground surface is significantly increased by about 50% under 3-point bending compared with the 4-point bending test. This increase is due to the complete relaxation of the tensile initial residual stresses acting at the sur-

face. This plays a favourable effect in fatigue strength. The 3-point bending fatigue limit of the ground specimen reaches approximately the 4-point bending limit of the electropolished specimen.

The influence of stabilized residual stresses on fatigue limits of the AISI 316L steel ground specimens was predicted using the Dang Van's multiaxial criterion [43]. This criterion is expressed (Eq. (7)) by the limitation of an equivalent stress.

$$\sigma_{eq} \equiv \tau^a + \alpha_0 P_{\max} \leqslant \beta_0 \tag{7}$$

where τ^a et P_{max} are calculated from the applied cyclic stress tensor at the fatigue crack nucleation site. α_0 and β_0 are two material's constants that can be identified from two fatigue limits of the base material. In this work, the fatigue limits of the electro-polished specimens under the 4-point bending with two different loading ratios were used. The identified values are: $\alpha_0 = 0.14$ and $\beta_0 = 171$ MPa.

The difference between experimental and predictive results is evaluated by the fatigue strength indicator proposed in [22]. The in-depth variation of this indicator is expressed as follows:

$$I(z) = \frac{\sigma_{eq}(z) - \beta_0}{\beta_0} \times 100 \tag{8}$$

The grinding residual stresses are superposed to the cyclic stresses resulting from both the 3-point or the 4-point bending test. The deduced total stresses acting at the notch root of specimens (the crack initiation site) were evaluated at the stabilized state using the FE models presented in Section 4. These stresses were used after to calculate the equivalent stress of the Dang Van's criterion.

The calculated profiles of the fatigue strength indicator, for both 3-point and 4-point bending fatigue limits, are illustrated in Fig. 19. In the two cases, the maximum values of this indicator are situated at the surface. This result predicts that the fatigue cracks initiate at the surface accordance with the experimental observations. Furthermore, it should be noted that the predictive calculation is almost exact in the case of 3-point bending ($I_{3p}(0) = +2\%$), while it is slightly not conservative in the case of 4-point bending ($I_{4p}(0) = -7\%$). These results show the important role played by the stabilized surface residual stresses on bending fatigue strength of the ground surface made of AISI 316L steel. In fact, the Dang Van's criterion allows predicting the fatigue limit with a satisfactory accuracy when only the stabilized surface residual stresses are taken into account. As a result, the combined effect of roughness and surface hardening seems to be lower.

The surface hardening is generally beneficial for the fatigue strength by retarding the crack fatigue initiation [5]. This effect can be evaluated by correction of the β_0 constant in the Dang Van's criterion according to the model presented by Fathallah et al. [22]. On the contrary, the surface roughness plays a detrimental effect on fatigue strength [44,45]. In fact, the machining grooves induce very local stress concentrations which accelerate the fatigue crack nucleation. This effect depends strongly on many factors such as morphology and size of surface defects, material hardness, and loading direction. Generally, it presents lower levels in the case of ductile materials explained by the cyclic plasticity in the vicinity of surface defects. According to Arola et al. [45], the roughness effect can be treated as a notch effect and evaluated by the fatigue stress concentration factor (K_f). This approach has been validated in the case of AISI 4130 CR steel specimens machined by the abrasive waterjet technique. The surface texture resulting from machining was characterized by an average roughness (R_a) situated between 1.96 and 6.04 μm. The predictive values of the factor K_f were found within 2% of the apparent values estimated from experimental results in the range from 1.01 to 1.08.

6. Conclusion

The aim of the present paper was to evaluate experimentally and numerically the residual stress relaxation and its effect on the fatigue strength of AISI 316L steel ground surfaces in comparison to electro-polished ones. These evaluations were conducted using bending fatigue tests with the 3-point and 4-point configurations ($R_\sigma = 0.1$) on notched specimens, residual stress measurements and FE analyses of residual stress relaxation. The following conclusions can be drawn.

(1) The 4-point bending fatigue limit at 2×10^6 cycles of ground specimens is lower of ≈−35% than that of the electro-polished ones. This degradation is associated with a slight relaxation of residual stresses which remain tensile stresses. While under the 3-point bending test, the surface residual stresses relax completely and provoke a significant increase of the fatigue limit of ≈50% compared to that of the 4-point bending.

(2) The residual stress relaxation under each bending mode has been simulated using a 2D FE model which takes into account the initial state and the cyclic hardening behaviour of the ground layer. The base material model can be calibrated with a satisfactory precision using the results of LCF tests, while the material model for the surface layer can be calibrated by adjusting the numerical values of the stabilized residual stresses with their experimental values.

(3) The difference of residual stress relaxation between the 3-point and the 4-point bending tests is explained by the effect of stress concentration on the cyclic hardening behavior of the notch root of ground specimens. Numerical analysis show that the stabilization of residual stresses is occurred after the first cycle for the 4-point bending test corresponding to the higher stress concentration ($K_{t\text{-}4p} = 1.66$), while it requires many cycles for the 3-point bending test corresponding to the lower stress concentration ($K_{t\text{-}3p} = 1.54$).

(4) The incorporation of the stabilized residual stresses with the applied cyclic stresses in the Dang Van's criterion has allowed to predict with an acceptable accuracy the fatigue limits under both 3-point and 4-point bending tests. This confirms that the influence of grinding residual stresses on fatigue strength of the AISI 316L steel surfaces is more important than the combined effect of superficial hardening and roughness.

References

[1] Totten G, Howes M, Inoue T. Handbook of residual stress and deformation of steel. Materials Park, Ohio: ASM International; 2002.

[2] Brand A, Flavenot JF, Gregoire R, Tournier C. Données technologiques sur la fatigue, 3ème éd. Centre techniques des industries mécaniques (CETIM); 1992.

[3] Wagner L. Mechanical surface treatments on titanium, aluminum and magnesium alloys. Mater Sci Eng 1999;A263:210–6.

[4] Webster GA, Ezeilo AN. Residual stress distribution and their influence on fatigue lifetimes. Int J Fatigue 2001;23:375–83.

[5] Sasahara H. The effect on fatigue life of residual stress and surface hardness resulting from different cutting conditions of 0.45% C steel. Int J Mach Tools Manuf 2005;45:131–6.

[6] Gao Y, Li X, Yang Q, Yao M. Influence of surface integrity on fatigue strength of 40CrNi2Si2MoVA steel. Mater Lett 2007;61:466–9.

[7] Cao W. Adoucissement cyclique des aciers et relaxation des contraintes résiduelles de grenaillage en fatigue. PhD thesis. ENSAM d'Aix-en-Provence, France; 1989.

[8] Meguid SA, Hammond DW. Fatigue fracture and residual stress relaxation in shot peened components. In: Proc sec int conf on residual stresses. Amsterdam; 1989. p. 797–802.

[9] Torres MAS, Voorwald HJC. An evaluation of shot peening, residual stress and stress relaxation on the fatigue life of AISI 4340 steel. Int J Fatigue 2002;24:877–86.

[10] Sidhom N, Laamouri A, Fathallah R, Braham C, Lieurade HP. Fatigue strength improvement of 5083 H11 Al-alloy T-welded joints by shot peening:

experimental characterization and predictive approach. Int J Fatigue 2005;27:729–45.
[11] Juijerm P, Altenberger I, Scholtes B. Fatigue and residual stress relaxation of deep rolled differently aged aluminium alloy AA6110. Mater Sci Eng 2006;A426:4–10.
[12] Nikitin I, Besel M. Correlation between residual stress and plastic strain amplitude during low cycle fatigue of mechanically surface treated austenitic stainless steel AISI 304 and ferritic–pearlitic steel SAE 1045. Mater Sci Eng 2008;A491:297–303.
[13] Dalaei K, Karlsson B, Svensson LE. Stability of shot peening induced residual stresses and their influence on fatigue lifetime. Mater Sci Eng 2011;A528:1008–15.
[14] Löhe D, Vöhringer O. Stability of residual stresses. In: Totten G, Howes M, Inoue T, editors. Handbook of residual stress and deformation of steel. Materials Park, Ohio: ASM International; 2002. p. 54–69.
[15] Denkena B, Köhler J, Breidenstein B, Mörke T. Elementary studies on the inducement and relaxation of residual stress. Procedia Eng 2011;19:88–93.
[16] Flavenot JF, Skalli N. Effect of grinding conditions on fatigue behavior of 42CD4 grade steel; comparison of different fatigue criteria incorporating residual stresses. In: Mordfin L. editor. Mechanical relaxation of residual stresses. ASTM STP 993. Philadelphia; 1988. p. 91–111.
[17] Kodama S. The behaviour of residual stress during fatigue stress cycles. In: Proceedings of the international conference on mechanical behaviour of materials II, society of material science, Kyoto, Japan; 1972. p. 111–18.
[18] Deperrois A. Calcul de la limite d'endurance des aciers. PhD thesis. France: Ecole polytechnique Paris; 1991.
[19] Akrache R. Prévision de la durée de vie en fatigue des structures 3D par la méthode des éléments finis. PhD thesis. France: Université de Technologie de Compiègne; 1998.
[20] Arbab Chirani S. Méthodologie pour la prise en compte des contraintes résiduelles dans un calcul prévisionnel de durée de vie en fatigue de pièces en aluminium. PhD thesis. France: Université de Technologie de Compiègne; 1998.
[21] Gong K, Milley A, Lu J. Design tool on fatigue for 3D components with consideration of residual stresses. SAE 2001 world congress, fatigue research & applications (Part A&B), Detroit, MI, USA; 2001. p. 1–6.
[22] Fathallah R, Laamouri A, Sidhom H, Braham C. High cycle fatigue behavior prediction of shot-peened parts. Int J Fatigue 2004;26:1053–67.
[23] Benedetti M, Bortolamedi T, Fontanari V, Frendo F. Bending fatigue behaviour of differently shot peened Al 6082 T5 alloy. Int J Fatigue 2004;26:889–97.
[24] Benedetti M, Fontanari V, Scardi P, Ricardo CLA, Bandini M. Reverse bending fatigue of shot peened 7075-T651 aluminium alloy: the role of residual stress relaxation. Int J Fatigue 2009;31:1225–36.
[25] Zhuang WZ, Halford GR. Investigation of residual stress relaxation under cyclic load. Int J Fatigue 2001;23:31–7.
[26] Seungho H, Lee T, Shin B. Residual stress relaxation of welded steel components under cyclic load. Mater Technol (Steel Res) 2002;73:414–20.
[27] Maximov JT, Duncheva GV, Mitev IN. Modeling of residual stress relaxation around cold expanded holes in carbon steel. J Constr Steel Res 2009;65:909–17.
[28] Zaroog OS, Aidy A, Sahari BB, Zahari R. Modeling of residual stress relaxation: a review. J Sci Technol 2009;17:211–8.
[29] Zaroog OS, Aidy A, Sahari BB, Zahari R. Modeling of residual stress relaxation of fatigue in 2024-T351 aluminum alloy. Int J Fatigue 2011;33:279–85.
[30] Liu J, Yuan H. Prediction of residual stress relaxations in shot-peened specimens and its application for the rotor disc assessment. Mater Sci Eng 2010;A527:6690–8.
[31] Lu J, Flavenot JF, Turbat A. Prediction of residual stress relaxation during fatigue. In: Mordfin L. editor. Mechanical relaxation of residual stresses. ASTM STP 993. Philadelphia; 1988. p. 75–90.
[32] Smith DJ, Farrahi GH, Zhu WX, McMahon CA. Experimental measurement and finite element simulation of the interaction between residual stresses and mechanical loading. Int J Fatigue 2001;23:293–302.
[33] Bertini L, Fontanari V, Straffelini G. Influence of post weld treatments on the fatigue behaviour of Al-alloy welded joints. Int J Fatigue 1998;20:749–55.
[34] Boyce BL, Chen X, Peters JO, Hutchinson JW, Ritchie RO. Mechanical relaxation of localized residual stresses associated with foreign object damage. Mater Sci Eng 2003;A349:48–58.
[35] Lu J. Handbook of measurement of residual stresses. The Fairmont Press Inc.; 1996.
[36] Noyan IC, Cohen JB. Residual stress. Measurement by diffraction and interpretation. Springer-Verlag; 1987.
[37] Collins JA. Failure of materials in mechanical design – analysis prediction and prevention. New York, USA: John Wiley & Sons, Inc.; 1993.
[38] Lee YL, Pan J, Hathaway R, Barkey M. Fatigue testing and analysis – theory and practice. Boston, USA: Elsevier Inc.; 2005.
[39] Hibbit, Karlsson and Sorensen Inc. ABAQUS version 6.5; 2005.
[40] Moussavi Toorshizi SE. Ecrouissage cyclique d'aciers inoxydables austénitique, ferritique et austéno-ferritique: influence de l'histoire de chargement. PhD thesis. France: Université de Sciences et Technologie de Lille 1; 1997.
[41] Ye D, Matsuoka S, Nagashima N, Suzuki N. The low-cycle fatigue, deformation and final fracture behaviour of an austenitic stainless steel. Mater Sci Eng 2006;A415:104–17.
[42] Lemaitre J, Chaboche JL. Mécanique des matériaux solides. Dunod, Paris; 2001.
[43] DangVan K. Introduction to fatigue analysis in mechanical design by the multiscale approach. In: DangVan K, Papadoupoulos IV, editors. High cycle metal fatigue in the context of mechanical design, CISM courses and lectures no. 392. Springer-Verlag; 1999. p. 57–88.
[44] Novovic D, Dewes RC, Aspinwall DK, Voice W, Bowen P. The effect of machined topography and integrity on fatigue life. Int J Mach Tools Manuf 2004;44:125–34.
[45] Arola D, Williams CL. Estimation the fatigue stress concentration factor of machined surfaces. Int J Fatigue 2002;24:923–30.